Icarus 230 (2014) 81–95

Contents lists available at ScienceDirect

Icarus

journal homepage: www.elsevier.com/locate/icarus

Constraints on Mars' recent equatorial wind regimes from layered deposits and comparison with general circulation model results

E. Sefton-Nash [a,*], N.A. Teanby [b], C. Newman [c], R.A. Clancy [b], M.I. Richardson [c]

[a] Department of Earth and Space Sciences, University of California Los Angeles, 595 Charles Young Drive East, Los Angeles, CA 90095, USA
[b] School of Earth Sciences, University of Bristol, Queen's Road, Bristol BS8 1RJ, UK
[c] Ashima Research, 600 S. Lake Ave., Suite 104, Pasadena, CA 91106, USA

ARTICLE INFO

Article history:
Received 30 March 2013
Revised 6 November 2013
Accepted 11 November 2013
Available online 20 November 2013

Keywords:
Aeolian processes
Atmospheres, dynamics
Geological processes
Mars, climate
Mars, surface

ABSTRACT

Aeolian modification has been a fundamental surface process on Mars throughout the Amazonian. Orientations of aeolian features such as bedforms and yardangs are controlled by the prevailing wind regime during the feature's formation. Therefore, observation of recently formed bedform orientations provides a way to probe Mars' recent wind regime and constrain/test general circulation models (GCMs). We collect statistical distributions of transverse bedform and yardang azimuths at nine sites on Mars, and compare measured feature orientations to those predicted by using vector wind field output from the MarsWRF GCM.

We focus on layered deposits because their erodible nature makes them applicable to determination of Mars' modern wind regime. Our methods of mapping from the long-term wind field to predicted feature orientations include consideration of wind stress thresholds for sand movement to occur, sand flux equations, and the direction of maximum gross bedform-normal transport. We find that all methods examined typically agree with each other to within $\sim 15^{\circ}$, though there are some exceptions using high order wind stress weightings with multi-directional annual wind fields. Generally, use of higher wind stress thresholds produces improved matches to bedform orientations.

Comparison of multiple yardang orientations to annually variable wind fields is accomplished by inspection of directional maxima in modelled wind vector frequency distributions. Yardangs match well to model predictions and sub-populations in close proximity to each other are shown to match individual directional maxima in GCM output for a single site, implying that topographic effects may produce very localised unidirectional wind fields unresolved by the GCM.

© 2013 Elsevier Inc. All rights reserved.

1. Introduction

Aeolian features on Mars' surface are transient on a range of timescales. Relatively short-lived features such as wind streaks and active dunes are representative of present-day surface wind regimes, while less transient features such as yardangs and transverse aeolian ridges are a product of the time-integrated, changing wind regimes over longer timescales. In this study we compare orientation distributions of bedforms and yardangs to examine agreement between their inferred formative wind fields.

Aeolian feature orientations, morphology, and (in the case of active bedforms) movement may be used to infer aspects of the wind environment in which they formed. While some information may be extracted without employing atmospheric models at all (e.g., Ewing et al., 2010), additional insight can often be gained by comparing with model results, whether they are global (~degree scale) general circulation models (GCMs) or high-resolution (~km scale) mesoscale models. Equivalently, comparison between observed aeolian features and predicted surface wind fields can be used to validate the capability of a present day atmospheric model (if the bedforms are known to be currently active) or even to assess a paleo-climate simulation. A simple comparison of dune faces with model-predicted present-day prevailing/dominant winds (e.g., Fenton et al., 2005; Hobbs et al., 2010) provides a basic means of assessing whether dunes are currently active or may have formed in a past wind environment. However, because aeolian features are produced according to the time-integrated effect of the full wind field in a non-linear manner, more complex approaches have also been used that combine model output with dune formation theory to map winds to aeolian features, and predict, e.g., the movement and orientation of sand dunes. For Mars, modelled wind fields have been used in this way at global scales (e.g., Hayward et al., 2009) and also for some mesoscale (~km resolution) regions (e.g., Fenton et al., 2012; Newman et al., 2012). Previous comparisons of aeolian feature orientations with those predicted from Mars GCMs

* Corresponding author.
E-mail address: e.sefton-nash@uclmail.net (E. Sefton-Nash).

0019-1035/$ - see front matter © 2013 Elsevier Inc. All rights reserved.
http://dx.doi.org/10.1016/j.icarus.2013.11.014

(Haberle et al., 1993; Greeley et al., 1993; Gardin et al., 2012) have shown that there is often not agreement between modelled present-day wind vectors and those inferred from the orientations of aeolian features, at least when rather straightforward mappings between winds and aeolian features are assumed (e.g., when yardang orientations are compared to the seasonally-averaged wind directions predicted by a GCM). Climate forcing by the combination of orbital eccentricity cycles and precession of Mars spin axis (Ward, 1979a) has been shown by Fenton and Richardson (2001) not to cause sufficient change to surface wind fields to account for the observed disagreement, for obliquity <45°. More significant changes to the surface wind field have been noted for obliquities exceeding 45° (Newman et al., 2005). It has also been suggested that changes to local topography, climate or polar wander may also have occurred (Fenton and Richardson, 2001). However, several other factors may also contribute to the disparity, including (but not limited to): (i) low GCM resolution compared to local topographic variation (meaning that the model cannot properly capture the feature-forming wind field); (ii) uncertainty in properties that can influence erosive or depositional behaviour and therefore feature orientation (such as sediment availability, grain size distributions, and fine-scale surface roughness), or (iii) choice of numerical technique employed to map GCM surface wind vectors to predicted feature orientation (see Section 3.2). Hayward et al. (2009) found a better match between modelled wind directions and slip face orientations using a mesoscale model than with a GCM, demonstrating the likely importance of (i) – i.e., increased atmospheric model resolution which we intend to pursue in future work (see Sections 5 and 6). The uncertainties listed in (ii) are certainly likely to be important too, but require data that are unavailable at this time. In this work, we therefore focus on (iii) i.e., the methods by which we map from model wind stresses to predicted feature orientations. The selection of appropriate numerical relationships to use here is impeded by gaps in our understanding of sediment transport, formation of bedforms, and rock erosion, both for Mars and in general.

Surface wind dynamics and erosion rates on Mars differ greatly from those on Earth, but relationships developed through field observation, laboratory experiments, and modelling form the basis for much of our understanding of aeolian processes on Mars (e.g., Bagnold, 1941; Greeley et al., 1982; Bitter, 1963a,b; Merrison et al., 2008; Rubin and Hunter, 1987). More recently, in situ and orbital observations have yielded erosion and sediment transport rates in selected locations (Sullivan et al., 2005; Bourke et al., 2008; Golombek et al., 2010; Fenton, 2006; Silvestro et al., 2010, 2011, 2013; Bridges et al., 2012a,b).

Whereas some aspects of Mars' erosional environment are well-constrained, others are largely unknown (e.g., sediment availability, grain-size distributions and material strength). In an attempt to better understand the remaining disparities between predicted and observed aeolian features, we test a range of numerical mappings between wind vectors output by the MarsWRF GCM (Richardson et al., 2007; Toigo et al., 2012) and predicted bedform orientations (see (iii) above). These are described in detail in Section 3.2; here we merely note that the formation mechanisms for bedforms (depositional features) and yardangs (erosional features) are very different. Bedforms and yardangs will therefore reflect different aspects of the wind regime and thus different weightings, or numerical mappings, of the GCM outputs.

Bedforms are initially built from scratch via the accumulation of sand, while yardangs are produced by the removal of rock material from around the sides of an existing feature as the wind is deflected around it. As an example, we would expect a unidirectional wind field to produce transverse dunes (or barchan where sand supply is limited) with crests oriented normal to the wind direction, but we would expect the same wind field to produce yardangs oriented parallel to the wind direction, i.e., at 90° to the dunes. For more complex wind regimes, however, theory suggests that dunes will form with an orientation that maximises gross bedform-normal transport (GBNT) of sediment (Rubin and Hunter, 1987) (see Sections 2.2 and 3.2), while yardang orientations may perhaps be more controlled by the dominant sediment carrying wind direction (see Section 2.3). Thus a 90° offset between bedform and yardang orientations need not generally occur.

In this study we use the term 'bedforms' to refer to features that may include transverse dunes and transverse aeolian ridges (TARs), that may or may not be active under present-day wind regimes (Balme et al., 2008; Zimbelman, 2010) (also see Section 2.2). It is unclear whether TARs originate as small dunes (formed by saltation) or large ripples (formed by creep), but in either case their transverse and sedimentary nature suggests that their orientation should be controlled by GBNT, and upper limits on their age may be constrained by the crater retention age of their host surface.

We compare our predictions to the observed populations of bedforms and yardangs at nine sites (Figs. 1 and 2) selected for their highly wind-eroded nature. Sites are constrained to locations of fine layered deposits (FLDs), which occur predominantly at low latitudes, have highly eroded sedimentary surfaces, young crater retention ages and are typically elevated above the surrounding terrain (Catling et al., 2006; Okubo et al., 2008; Sefton-Nash et al., 2012; Warner et al., 2011) making them more susceptible to erosion by oncoming winds due to topographic forcing.

In order to place upper limits on the age of the least transient wind-eroded features, we also derive model crater retention age fits to established isochrons for young surfaces with populations of small diameter craters (Hartmann, 2005). This study benefits from the use of high resolution (25–60 cm pixel^{-1}) images acquired by the High Resolution Imaging Science Experiment (HiRISE) (McEwen et al., 2007, 2010) instrument on Mars Reconnaissance Orbiter (MRO), which resolves small diameter craters and fine detail on eroded surfaces.

2. Study sites

2.1. Fine layered deposits

FLDs, also referred to as interior layered deposits (ILDs) if in chaotic terrains, are easily eroded deposits characterised by their high albedo, visible layering at a variety of scales and low crater densities (Lucchitta et al., 1992; Catling et al., 2006; Okubo, 2010; Ansan et al., 2011; Flahaut et al., 2010; Fueten et al., 2010; Sefton-Nash et al., 2012). Regardless of their formative mechanism, their most recent history has been dominated by aeolian modification (e.g., Fig. 3B). FLDs have been identified in chaotic terrain, crater interiors, among spur-and-gully wall units, and inter-crater terrain (Malin and Edgett, 2000; Chojnacki and Hynek, 2008), but are generally confined to the martian tropics and subtropics. FLDs are commonly elevated above the surrounding terrain which, combined with their generally friable nature, likely makes their surfaces accurate recorders of recent wind directions.

2.2. Identifiable aeolian features I: bedforms

Aeolian bedform type is largely determined by the wind regime and the availability of mobile material. Martian dunes (Fig. 3E and F) are mostly transverse and crescentic (barchans). Rare dune types include longitudinal (Breed et al., 1979; Lee and Thomas, 1995; Hayward et al., 2007) and star (Edgett and Blumberg, 1994) dunes, which indicate predominantly unidirectional (McKee, 1979) and multi-directional wind regimes, respectively.

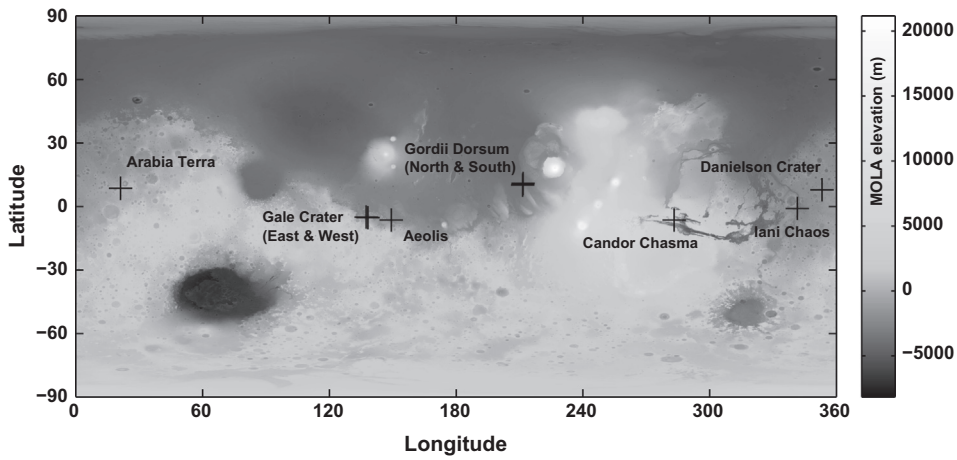

Fig. 1. Location of sites selected for this study. Reference map is MOLA 32ppd topography Zuber et al. (1992).

Where more complex wind regimes exist, the GBNT hypothesis proposes that bedforms will form with a crest orientation such that the total ('gross') sediment transport normal to the crest is maximised, where total refers to transport from both sides of the crest (Rubin and Hunter, 1987). The use of gross rather than net transport reflects the idea that, for example, an E–W oriented crest will grow higher if equal amounts of sediment accumulates there from the north as from the south, despite the net transport in that case being zero. There is growing evidence that this approach works well on Earth for both aeolian and sub-aqueous bedforms (e.g., Lancaster, 1991; Anthonsen et al., 1996; Lancaster et al., 2010; Reffet, 2008; Rubin et al., 2008; Wu et al., 2009), though disagreement has been noted in some situations or regions (e.g., Lancaster, 1991; Clarke et al., 2008; Derickson et al., 2008).

Estimates of aeolian transport rates on Mars are complicated by a lack of ground truth measurements. Earlier orbital studies concluded that due to Mars' thin atmosphere, wind velocities required to initiate saltation are much higher on Mars than on Earth (Greeley and Iversen, 1985), with measured and modelled surface wind speeds on Mars appearing to rarely exceed the estimated saltation threshold (Moore, 1985). However, the occurrence of major dust storms every few years (with the majority of dust injection presumed to occur via saltation of sand-sized particles, (e.g., Cantor et al., 2006) suggests a far more active aeolian environment. In addition, while the majority of large martian bedforms appear to be relatively stable and inactive, recent analysis of high resolution images shows substantial dune activity/migration in isolated areas (Bourke et al., 2008; Bridges et al., 2012a,b; Chojnacki et al., 2011; Silvestro et al., 2010, 2013), and in some cases with migration rates similar to those found on Earth (Bridges et al., 2012b).

The apparent shortfall in modelled winds may be due to their having come from GCMs, which run at a few degrees resolution and thus cannot resolve strong, localised wind gusts that have the greatest influence on transport and erosion (Bridges et al., 2012a). Hysteresis effects (Kok, 2010), i.e., the ability to maintain saltation at much lower wind stresses (which must only exceed the impact threshold) once the higher fluid threshold has been exceeded – may also greatly impact these estimates. For active dunes, the length of time taken for a dune to migrate its own length is described as the turnover time (Andreotti et al., 2002), and provides an estimate of the time period over which the dune was formed. Recent modelling of transport properties under Mars surface conditions suggested dune migration rates of a few centimetres per thousand years (Claudin and Andreotti, 2006).

However, observations at sites located from the equator to mid-latitudes indicate common dune and ripple migration rates of 0.01–4.5 m year^{-1} (Fenton, 2006; Silvestro et al., 2011, 2013; Bridges et al., 2012a,b), indicating that more rapid bedform migration occurs in some areas under present-day conditions. This allows comparatively rapid turnover times on the order of decades for a typical 50 m wavelength dune. Therefore, active dunes may represent wind regimes of several decades duration based on observations, although significant uncertainty exists.

However, the martian surface harbours a combination of rapidly migrating dunes that are active in the present-day wind regime, slowly migrating dunes that formed during past climate epochs (e.g., as shown at Meridiani Planum by Golombek et al., 2010) and TARs. TARs are low-order bedforms with similar wavelengths to dunes or large ripples (~20–70 m) (Balme et al., 2008; Bourke et al., 2003; Zimbelman, 2010). By comparison to transverse dunes, which are asymmetrical in cross-section and have a shorter lee slope than the stoss side, TARs appear symmetrical in cross section (Zimbelman, 2010). This morphological evidence, as well as surface observations at Meridiani Planum by the Mars Exploration Rover Opportunity (Sullivan et al., 2005, 2007) has lent support to the theory that some TARs are granule ripples, which require a constant source of sediment to remain active. This could help explain their frequent spatial association with large dark dunes (LDDs) (Balme et al., 2008). However, larger TARs (>0.5 m in height) have also been proposed to be reversing dunes (Zimbelman, 2010). In any case, determining the crater retention age of its host surface provides a method to place an upper limit on a features' age. This technique was applied to date TARs in the Meridiani region at 1–3 Ma (Berman et al., 2011).

In this study we do not distinguish between dunes and TARs and refer to them both under the general term 'bedform'. This is because without repeat observations (e.g., Silvestro et al., 2013) it is impossible to definitively distinguish between active and inactive bedforms, and there is insufficient temporal coverage at most of our sites to accomplish this. This is another reason we chose to use FLDs: we can constrain these easily erodible terrains to relatively young crater retention ages, meaning that yardangs and bedforms on them are relatively modern. Our analysis also avoided obviously eroded or cratered bedforms and all features had a fresh appearance. Therefore even if bedforms are not active, we can still expect them to be representative of Mars' modern wind field. Furthermore, because of continued erosion, the smaller vertical scale of bedforms compared to yardangs suggests they could be more sensitive to more recent winds, so the two types of formation may be sensitive to different timescales.

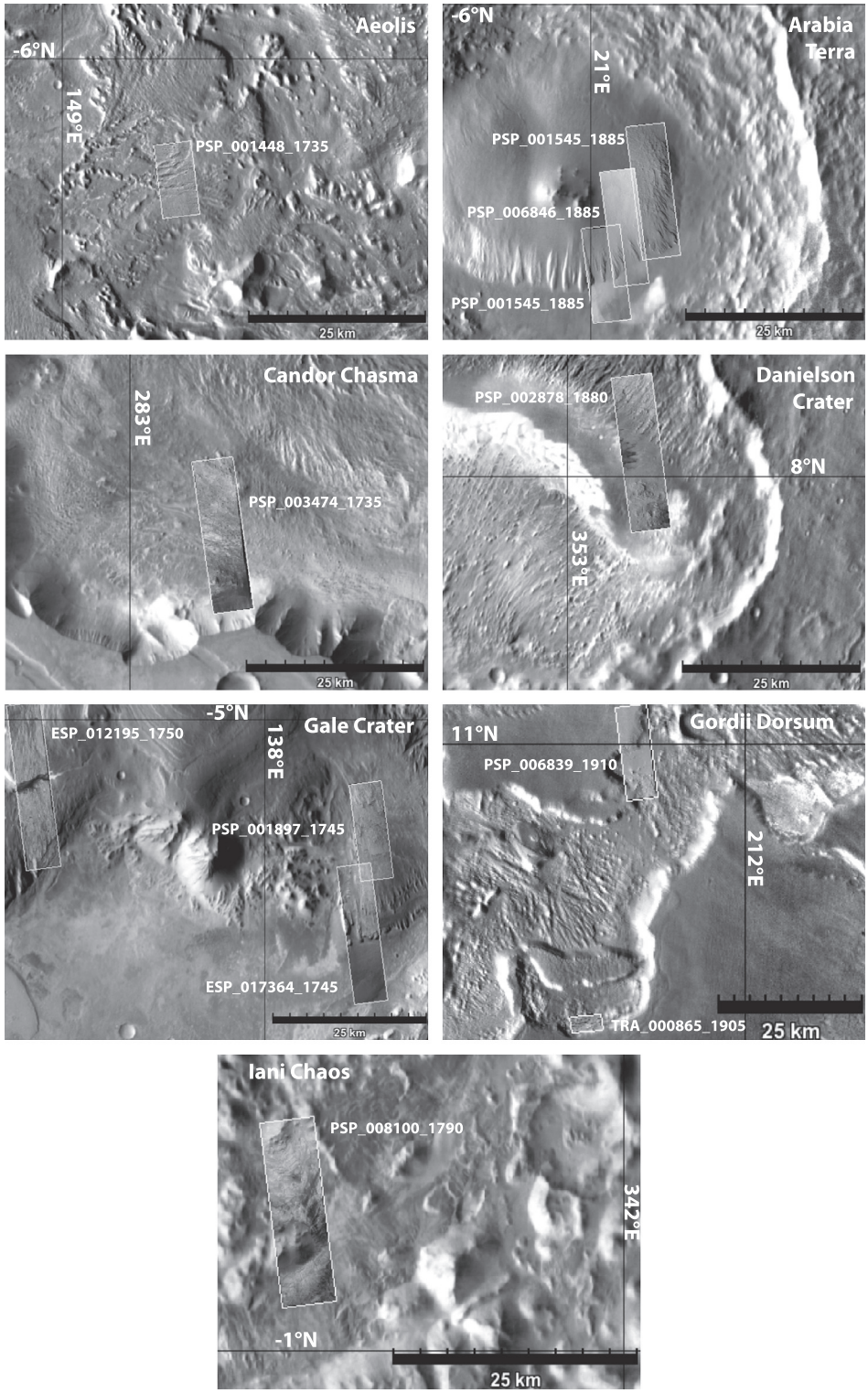

Fig. 2. Context of sites selected for this study. Rendered HiRISE stamps indicate our study areas. Background context basemap is from THEMIS daytime IR imagery.

2.3. Identifiable aeolian features II: yardangs

Yardangs are remnant, wind-eroded, aerodynamic ridges (Fig. 3A–D), which form parallel to the wind direction as the result of strong unidirectional wind regimes which cause abrasion and deflation of sedimentary rock into channels, which are then widened or streamlined (Greeley and Iversen, 1985; Ward, 1979b). Martian yardangs are larger and more elongated than their terrestrial counterparts (Bridges et al., 2007; de Silva et al., 2010). Yardangs are formed over longer timescales than bedforms and are predominantly found on terrains with young model crater retention ages, where erosive resurfacing produces low crater densities (e.g., FLDs).

The model crater retention age approximates an upper limit for the yardang formation timescale, with the caveat that very small craters may be resurfaced faster than large, topographically

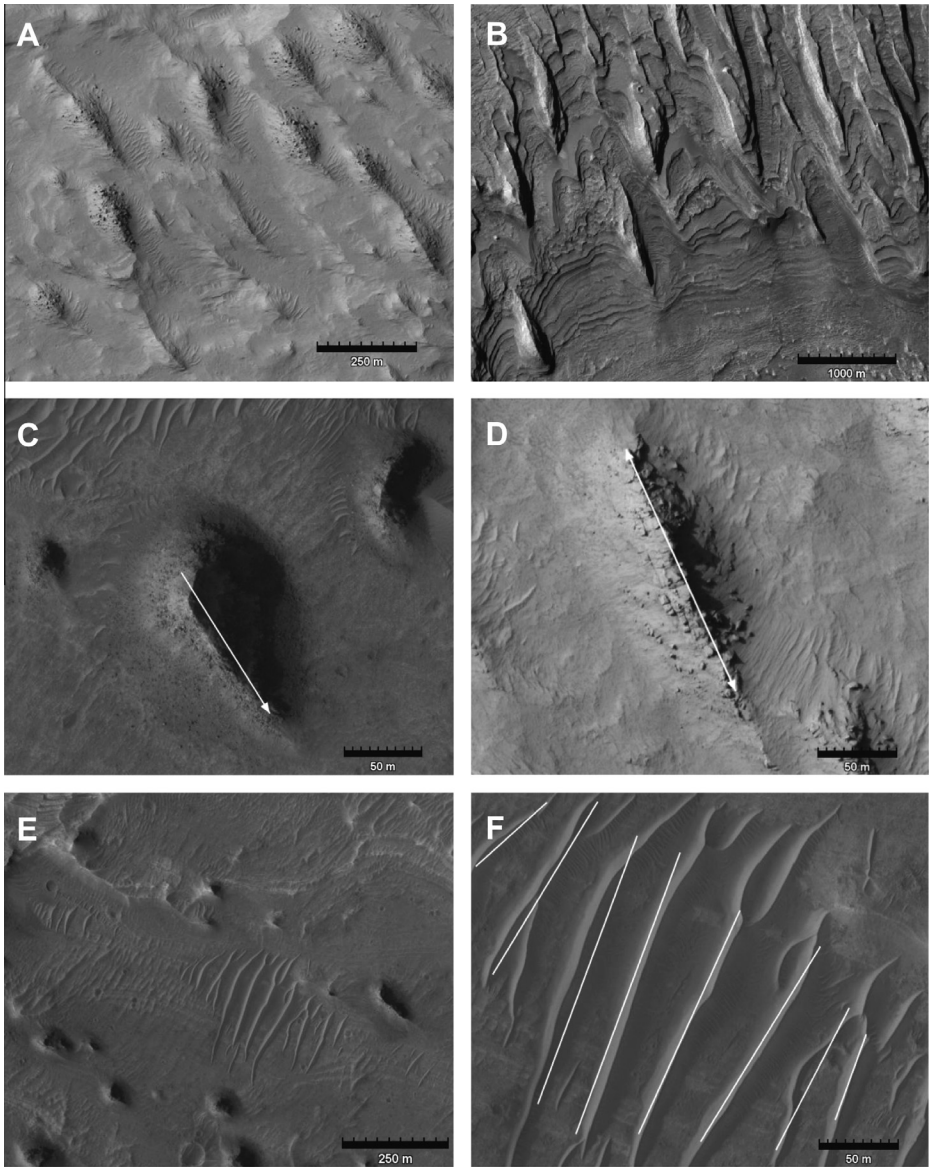

Fig. 3. Examples of yardangs and bedforms as seen in HiRISE images listed in Table 2. (A) Yardangs in Aeolis. (B) Elongate yardangs on layered terrain in east Gale crater (C) Teardrop-shaped yardang, allowing dominant wind direction to be inferred. (D) Symmetric yardang only allowing inference of wind direction with 180° ambiguity. (E) Bedforms in Candor Chasma. (F) Measurement of bedform crest trend, normal to inferred wind trend.

pronounced yardangs. Yardang long axis orientation is therefore indicative of recent, but not necessarily modern, wind regimes (Ward, 1979b).

2.4. Surface dating

In order to constrain the maximum age for aeolian features we date FLD surfaces at each site via crater counting using the HiRISE images shown in Fig. 2 and listed in Table 2. We aim only to determine order of magnitude estimates for maximum age, for which precise crater dating is not required to achieve. In any case, any more precise constraint of model surface ages is likely precluded by the uncertainties associated with estimating surface ages using small populations of small diameter craters. Uncertainties are greatest when only small ($D \lesssim 100$ m) craters are used (Hartmann, 2005). The crater production function for small diameter craters is complicated by secondary cratering (McEwen and Bierhaus, 2006), which, for young or freshly exposed surfaces, can increase apparent surface age with a relatively low number of impact events (McEwen et al., 2005). It is also unclear how the small crater population is affected by the strength of surface material (Dundas et al., 2010) and the temporal variability of the crater production function with spin axis obliquity and orbital eccentricity (Daubar et al., 2013).

Nonetheless, we estimate the order of magnitude upper limit of surface age at six sites that harboured a sufficient crater population to enable dating: Aeolis, Candor Chasma, Danielson crater, Gale crater (east), Gordii Dorsum (south) and Iani Chaos. FLD surfaces within HiRISE image footprints for sites at Arabia Terra, Gale crater (west) and Gordii Dorsum (north) showed the number of identifiable craters, N, to be fewer than 10, which we deemed inadequate for reliable crater statistics.

Error on crater retention age is typically constrained using the statistical variation between crater populations in separate areas on the same geologic unit (e.g., Warner et al., 2011). However, the small geographic area and young surface age of FLDs leads to generally low crater counts for this study. For statistical robustness we therefore treat counts for each site as one population. Error bars

in Fig. 4 represent $\sqrt{N}$, but an additional factor of two error should be considered, due to uncertainty in assigning model ages to isochrons Hartmann (1999). Isochrons represent model crater retention ages based on Hartmann (2005), which represents a refinement and synthesis of crater-dating techniques. This includes a correction applied to account for the loss of small bolides in Mars' atmosphere (Popova et al., 2003). However, in some cases fragmentation of bolides may work to increase apparent crater populations by production of clusters (Ivanov et al., 2008), which could in turn be misidentified as secondaries and therefore discounted. The loss of small craters due to deflation, abrasion and deposition is more likely than for larger craters, which have greater topographic expression. In general, the crater population represents the surface's crater retention age, an equilibrium between crater production and erasure weighted by the processes outlined above.

Deviation of our crater statistics from model age isochrons may be an indicator of uncertainties in crater production and erasure, particularly with regard to preferential resurfacing of small diameter craters because the sites we chose by definition must exhibit extensive aeolian modification. Craters $\gtrsim$ 50 m diameter in Candor Chasma (Fig. 4) may represent more rapid resurfacing of small craters compared to large diameter craters. However, we do not count large diameter craters in any other regions and this may simply be an artefact of the relatively small size of study areas.

We find most model surface ages relative to Hartmann (2005) isochrons for FLDs to span at least 0.1–10 Ma. Note that here 'model age' refers to the age since the surface was exposed to the atmosphere, rather than the age of the deposit. Low crater numbers often caused placement of lower error bounds close to zero years, i.e., present day. However, the absence of larger craters may artificially lower model ages. For comparison, Warner et al. (2011) calculated model ages for a group of FLDs in Iani Chaos, including the deposit we dated (with an upper error bar of ~9 Ma), as $24.8^{+3.2}_{-3.3}$ Ma. Importantly, recent studies by Malin et al. (2006) and Daubar et al. (2013)) have shown that isochrons by Hartmann (2005) may underestimate surface ages. Model crater retention ages in Table 1 and Fig. 4 could therefore be underestimated by a factor of ~3 (in addition to the plotted statistical error in Fig. 4). This would therefore place upper limits on crater retention ages for our chosen FLDs between ~12–30 Ma.

It is unclear whether the decline in frequency of small diameter craters that we observe at most sites (Fig. 4) is due to a larger atmospheric ablation loss than predicted by Popova et al. (2003) or preferential aeolian resurfacing of small craters. In any case, the young crater retention ages suggest that the oldest features observed in these deposits will have been formed by relatively recent wind regimes. Assuming that bedforms may have formed in the vicinity or could have migrated from other locations, crater retention ages also place moderate constraints on the timing of bulk bedform migration.

3. Method

3.1. Measurement of feature orientation

For our nine sites in seven areas (Fig. 1) where heavily wind-eroded FLDs are present, we chose appropriate HiRISE footprints (Fig. 2) such that enough area was covered to produce adequate statistics of bedform/yardang fields. Details of feature counts, site locations and HiRISE product IDs are shown in Table 2.

Yardang orientation was determined by calculating the azimuth of a vector defined by the two endpoints of their long axis. In some sites yardangs showed a distinctive teardrop shape (e.g., Figs. 3C and 5), allowing inference of a unique wind direction. In other sites, yardangs with more elongated and parallel topography allowed only inference of a 180° ambiguous trend line (e.g., Fig. 3D).

Bedform populations at each site were found only to be transverse, with the exception of Gordii Dorsum (north) and Arabia Terra where no bedforms were present within the image footprint (Table 2). Bedform orientation was determined by measurement of the trend line parallel to the mean azimuth of each crest (Fig. 3F). If bedforms are symmetrical and formed under a unimodal wind regime, then normals to their slip-faces should lie in a plane containing the formative wind direction. Because we do

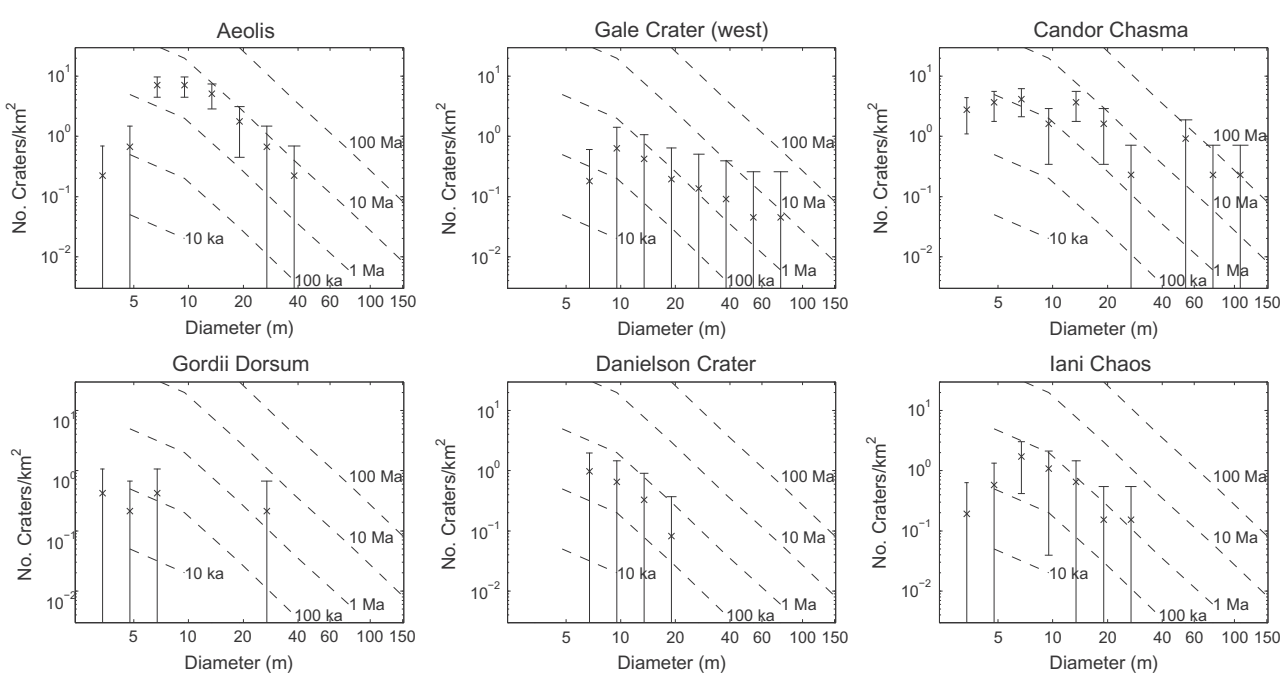

Fig. 4. Comparison of crater populations at each of the six sites with isochrons from Hartmann (2005). Error bars are $\sqrt{N}$. An additional factor of two error (not plotted) is suggested by Hartmann (1999) due to the uncertainty in assigning absolute ages to isochrons. However in addition, recent work by Malin et al. (2006) and Daubar et al. (2013) suggests surface ages derived using Hartmann (2005) isochrons could be underestimated by a factor of ~3. See Table 1 for crater counting statistics and age estimates.

Table 1
Crater count statistics and age estimates for each of the six sites with sufficient crater populations. Crater counts at Arabia Terra, Gale crater (west and south), and Gordii Dorsum (north) are not reported as they showed fewer than 10 countable craters. See Fig. 4 for comparison of crater populations with isochrons from Hartmann (2005), which were used to derive the model crater retention ages. Based on recent work by Malin et al. (2006) and Daubar et al. (2013) surface ages derived using Hartmann (2005) isochrons could be underestimated by a factor of ~3.

Site	No. craters	Area (km^2)	Hartmann (2005) age (Ma)
Aeolis	103	4.5	$\lesssim 10$
Candor Chasma	81	4.3	$\lesssim 50$
Danielson crater	25	12.2	$\lesssim 1$
Gale crater (west)	117	66.4	$\lesssim 50$
Gordii Dorsum (south)	12	9.4	$\lesssim 10$
Iani Chaos	118	26.0	$\lesssim 10$

Table 2
HiRISE image products inspected and number of yardangs and bedforms identified at each site.

Site	Lat.	Lon.	HiRISE product	Bedforms	Yardangs
Aeolis	−6.40	149.30	PSP_001448_1735	228	65
Arabia Terra	8.61	21.15	PSP_001545_1885	0	32
			PSP_003655_1885		
			PSP_006846_1885		
Candor Chasma	−6.40	283.20	PSP_003474_1735	129	131
Danielson crater	7.90	353.20	PSP_002878_1880	324	44
Gale crater (East)	−5.30	138.30	PSP_001897_1745	76	93
Gale crater (West)	−5.00	137.40	ESP_012195_1750	69	55
			ESP_017364_1745		
Gordii Dorsum (North)	10.90	211.70	PSP_006839_1910	0	96
Gordii Dorsum (South)	10.10	211.50	TRA_000865_1905	125	62
Iani Chaos	−0.90	341.50	PSP_008100_1790	590	72

not distinguish between dunes and TARs, inferred wind direction remains 180° ambiguous.

3.2. Mapping from GCM winds to predicted aeolian feature orientations

The MarsWRF GCM (Richardson et al., 2007) simulation used observationally-derived maps of surface features (e.g., topography, albedo) and the WBM radiative transfer scheme with the prescribed, time-varying MCD MGS atmospheric dust distribution, as detailed in Toigo et al. (2012). A $2^\circ \times 2^\circ$ horizontal resolution run, was sampled at the nine locations listed in Table 2 for each minute of a Mars year, giving a total of 963,360 wind vectors at each site, spread uniformly throughout the year. For each point we extracted zonal (u) and meridional (v) wind velocities, the friction velocity, u_*, and the atmospheric density, ρ. u and v were interpolated to an altitude of 1.5 m (the lowest model altitude was 10 m) using similarity theory (Monin and Obukhov, 1954). Wind speeds at 1.5 m were deemed representative of those that control transport via saltation. To account for a range of theories regarding the relationship between wind vectors and the resultant erosion and transport, we derive predicted bedform orientation from GCM output. We use two different numerical mapping approaches specific to bedforms and yardangs, both of which require construction of wind stress, σ, given by:

$$\sigma = \rho u_*^2 \tag{1}$$

For a wind with unit direction vector $\hat{\boldsymbol{x}}$, the particle transport flux $\boldsymbol{\tau}$ is defined by:

$$\boldsymbol{\tau} \propto \rho u_*^2 (u_* - u_{*t})\hat{\boldsymbol{x}} \qquad \text{if } u_* > u_{*t} \tag{2}$$

$$\boldsymbol{\tau} = 0 \qquad \text{otherwise}$$

where ρ is the air density, u_* is the friction velocity, and u_{*t} is the saltation threshold friction velocity, i.e., the minimum value required to initiate saltation from rest. To account for large annual variations in surface pressure on Mars we define a constant saltation threshold stress σ_t and use this to determine u_{*t} via $u_{*t} = \sqrt{\sigma_t/\rho}$.

3.2.1. Approach for bedforms

Our approach for bedforms is based on the observation that transverse bedform crests developed by a temporally dynamic wind field tend not to align normal or parallel to the direction of sediment transport, but to trend such that the maximum GBNT is achieved (Rubin and Hunter, 1987). We use a modified version of Rubin and Hunter (1987, 's) original approach, using the Fryberger flux in Eq. (2) to determine the transport and incorporating a saltation threshold as before. As a function of hypothetical bedform crest orientation, θ', defined clockwise from north, our modified GBNT, $T(\theta')$, is given by:

$$T(\theta') = \sum_{i=1}^{n} \rho_i u_{*i}^2 (u_{*i} - u_{*t}) \left| \frac{u_i \cos\theta' - v_i \sin\theta'}{\sqrt{u_i^2 + v_i^2}} \right| \quad \forall i \text{ where} : u_{*i} > u_{*t} \tag{3}$$

where the first term is the Fryberger transport flux and the second term is the absolute value of the transport flux direction vector projected into the bedform-normal direction. The optimum bedform crest orientation θ is then given by maximising $T(\theta')$. We solve this using a simple grid search in the range $0^\circ \leqslant \theta' < 180^\circ$ such that T is maximised for each site (Fig. 6).

Recent work has measured relative sand fluxes for the active Nili Patera dunes (Bridges et al., 2012a). By comparing the seasonal variations in Nili Patera sand fluxes with seasonal sand flux predictions by the MarsWRF GCM for different thresholds, we have determined that the best fit to the observed seasonal variation is produced for a threshold of 0.008 Pa (Ayoub (in preparation and personal communication), 2013). This is arguably the most direct method to date for constraining the most appropriate threshold to choose when using a GCM, which of course has relatively low

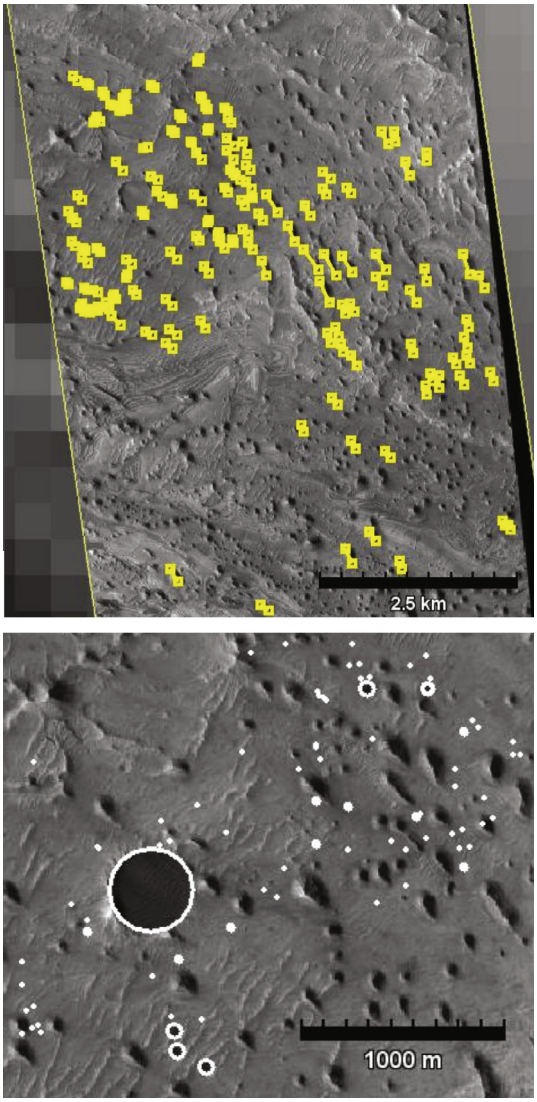

Fig. 5. Example measurements of feature orientation (upper) and crater counting (lower) in Candor Chasma.

spatial and temporal resolution compared to the fine scale, gusty winds that would actually be experienced by sand particles on Mars.

Therefore, to explore sensitivity to saltation threshold, we calculate predicted bedform crest line orientations θ for: zero stress threshold $\sigma_t = 0\ \mathrm{N\,m^{-2}}$; a moderate stress threshold $\sigma_t = 0.008\ \mathrm{N\,m^{-2}}$ and a higher threshold $\sigma_t = 0.016\ \mathrm{N\,m^{-2}}$. For comparison, $0.008\ \mathrm{N\,m^{-2}}$ corresponds to $u_{*t} \approx 0.7\ \mathrm{m\,s^{-1}}$ for an average martian surface air density. For sites where the GBNT function showed significant secondary maxima (observed only at Iani Chaos), we also show the expected bedform crest orientation for wind stress thresholds of $\sigma_t = 0.008\ \mathrm{N\,m^{-2}}$ and $\sigma_t = 0.016\ \mathrm{N\,m^{-2}}$ for the secondary GBNT peak.

3.2.2. Approach for Yardangs

We count MarsWRF surface wind vectors that are (i) unweighted, (ii) weighted by wind stress, and (iii) weighted by particle transport flux, in angular bins to illustrate the distribution of transport in annual wind fields that may contribute to yardang formation (Fig. 7). We determine the directions of primary and secondary maxima in these distributions to indicate the most likely yardang-forming erosion direction. In addition to weighting by Fryberger flux, we also investigate the impact of assuming that rock abrasion rates, which are responsible for producing yardangs, vary as u_*^5 rather than as u_*^3. In that case the 'particle transport flux' $\boldsymbol{\tau}$ (though it might more properly be referred to as an 'abrasion potential flux') has the relationship:

$$\boldsymbol{\tau} \propto \rho u_*^4 (u_* - u_{*t})\hat{\boldsymbol{x}} \tag{4}$$

This was suggested by the results of Anderson (1986), and can be thought of conceptually as the transported particle flux varying as u_*^3, with the erosion produced by particles impacting the rock face varying as u_*^2 (related to the kinetic energy of the particles). We refer to particle transport flux calculated in this manner as 'abrasion potential flux'.

4. Results

The orientations of transverse bedform trend lines and yardang long axes were measured at each site (e.g., Fig. 5). Azimuth distributions for each feature are plotted on Rose diagrams normalised to percentage of the total population for that feature (Figs. 8 and 9). The mean direction of yardangs (blue) and bedforms (red) should be approximately normal to each other if both populations were formed under the same unidirectional wind regime.

4.1. MarsWRF GCM output

To illustrate annual wind fields (Fig. 7) we count MarsWRF surface wind vectors in 64 angular bins and plot the normalised frequency of vectors: (1) unweighted; (2) weighted by the vector mean stress; (3) weighted by flux defined by Fryberger (1979) (Eq. (2); (4) weighted by Fryberger flux with a stress threshold $\sigma_t = 0.008\ \mathrm{N\,m^{-2}}$; (5) weighted by Fryberger flux with $\sigma_t = 0.016\ \mathrm{N\,m^{-2}}$, and (6) weighted by abrasion potential flux, where $\boldsymbol{\tau} \propto \rho u_*^4 (u_* - u_{*t})$ and $\sigma_t = 0.008\ \mathrm{N\,m^{-2}}$.

4.2. Bedforms

Transverse bedform crest orientations at each site are plotted as trend lines with 180° symmetry (Fig. 8). In Fig. 8 we show the predicted orientations of bedform trend lines calculated by the numerical formulations involving maximising GBNT (Eq. (3) for various wind stress thresholds. In the GBNT function for Iani Chaos we also show the orientation of a significant secondary maximum that is of comparable magnitude to the primary.

If MarsWRF wind vectors represent the present bedform-forming wind field and our chosen bedforms are representative of modern climate, then the predicted trend lines (red lines[1] in Fig. 8) should agree with the mean bedform crest trends observed.

4.3. Yardangs

When a yardang showed a tear drop morphology, a unique flow direction could be inferred (Fig. 9). 180° ambiguous yardangs were rare and typically numbered less than ~10%, but where they occured yardang direction was plotted in the same sense as neighbouring unambiguous yardangs, which were assumed to be exposed to similar wind fields. For Danielson crater, sufficient ambiguity was present for all yardangs that we plot them as 180° ambiguous trends.

The most likely yardang-forming erosion directions are plotted on Fig. 9 as the directions of principle and secondary maxima in weighted vector frequencies in Fig. 7. Secondary orientations in

[1] For interpretation of colour in Fig. 8, the reader is referred to the web version of this article.

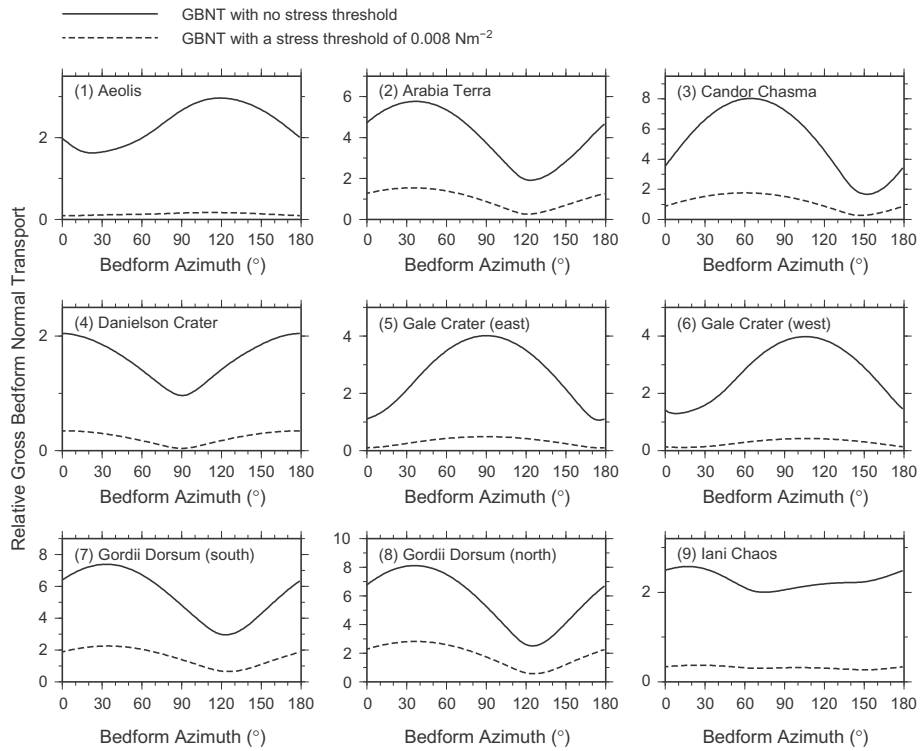

Fig. 6. GBNT Rubin and Hunter (1987) calculated by solving Eq. (3) over the 180° angular range of possible bedform trend line orientations.

dashed circles indicate vector frequency maxima that are present for low-order weightings, but that become subdued for higher order weightings of u_*^3 and u_*^5 (abrasion potential flux). Winds in these directions with lower erosive power may therefore be less likely to contribute to yardang formation.

If modelled wind fields are of the same orientation as those that formed measured yardang populations, then principle wind stress directions (numbers in Fig. 9) should match yardang long axis orientations.

5. Discussion

5.1. Bedforms and GBNT

Good matches are seen between bedforms and maximum GBNT at 4 of 7 sites: Danielson crater, Gale crater (east and west) and Gordii Dorsum south. Use of higher stress thresholds ($\sigma_t = 0.016\ \mathrm{N\ m^{-2}}$) typically improve matches where wind regimes are multi-directional. Sites where GBNT is less impacted by choice of threshold tend to show predominantly unidirectional wind regimes with respect to Fryberger flux (i.e., Danielson crater and both sites in Gordii Dorsum).

At Candor Chasma bedform orientations are within 15–30° of predicted and the match improves for progressively higher stress thresholds. At Iani Chaos the best match is seen for the highest threshold $0.016\ \mathrm{N\ m^{-2}}$, perhaps implying the threshold required to initiate sediment transport lies above this. However, Iani Chaos shows a low amplitude in GBNT over the total angular range (Fig. 6), implying a distribution of wind vectors from many directions over the course of the year, which is reflected in the angular dispersion of high vector frequencies in Fig. 7. Consequently, the direction of the second highest GBNT inflexion for Iani Chaos in Fig. 8 (black lines) also shows moderate agreement with observed bedform populations, but the apparent match is statistically insignificant. In any case, such a complex multi-directional wind field, is not consistent with simple transverse bedforms.

Aeolis shows the worst match between modelled and observed bedform orientations, with the maximum GBNT at all thresholds nearly perpendicular to the observed bedform orientations, as opposed to aligned with them. We discuss plausible reasons for this mismatch in Section 5.3.

5.2. Yardangs

There is good agreement for most regions between yardang long axis orientation and primary or secondary wind stress maxima, with the exception of Aeolis (Fig. 9). Arabia Terra yardangs are dispersed over about a 50° range, but match well with the secondary maximum, defined by low-order weighted and non-weighted peak in wind vector frequency. The direction of the primary transport flux maximum is offset from the edge of the yardang population by about ~15°. Candor Chasma also shows a good match to the secondary direction ('2' in dashed circle, Fig. 9). This direction is a maximum only if no wind stress weightings are included, i.e., although winds are predicted to occur often in this direction, their associated fluxes are predicted to be far weaker than those in the direction labelled '1'. Danielson crater could be regarded as a good fit if yardang sense were able to be constrained to a unique 180° angular range. Excellent matches are seen between predicted and observed yardang orientations at both sites in Gale crater. Both Gordii Dorsum south and north sites show similar offsets of ~10–20° between GCM dominant wind directions and yardangs, but bedforms (which are only present at the south site) show a better match to GBNT predictions from the GCM. Therefore Gordii Dorsum presents a reasonable case for further investigation into consistent offsets between bedforms and yardangs, which may yield information on wind field change if bedforms are modern and younger than yardangs, and if higher spatial resolution wind models produce similar predicted orientations. Yardangs poorly match GCM predicted orientations, as well as bedforms, at the Aeolis site, perhaps implying that higher-resolution modelling is required to resolve bedform- and

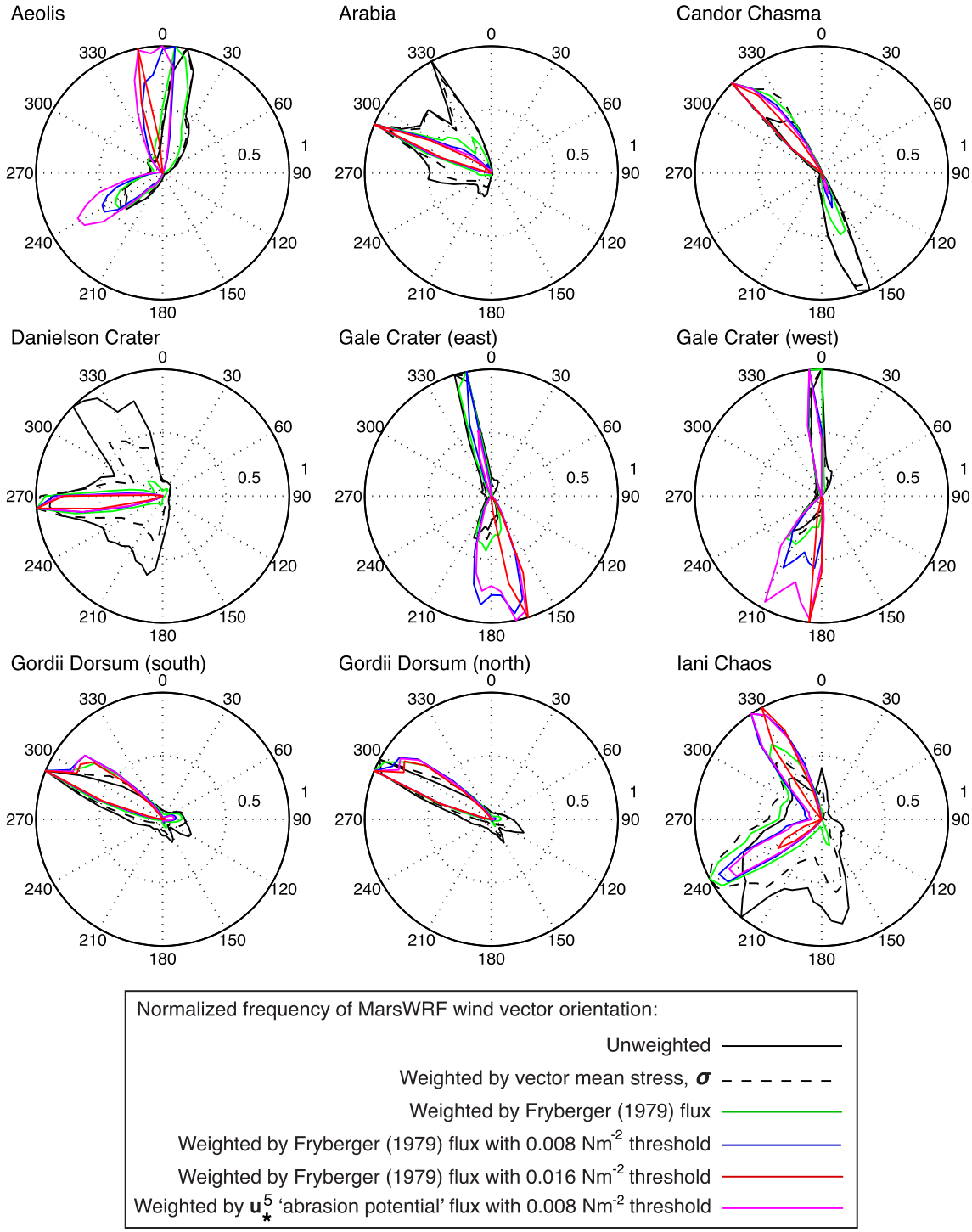

Fig. 7. Azimuth distribution of surface wind vectors produced by the MarsWRF GCM over one Mars year in the present climate regime. Lines are drawn between frequency counts in each of 64 bins of angular width 5.625°. Black solid lines are vector frequency in each bin. Dashed lines are weighted by wind stress, σ, which takes into account atmospheric density (Eq. (1)). Green, blue and red lines are calculated using Eq. (2) and magenta lines by Eq. (4). Unidirectional wind regimes persist at Gordii Dorsum while bi-directional wind regimes dominate at Aeolis, Candor Chasma and Gale crater. Annually variable multi-directional wind fields are present at Danielson crater and Iani Chaos. (For interpretation of the references to colour in this figure legend, the reader is referred to the web version of this article.)

yardang-forming winds (also see discussion of Aeolis in Section 5.3). In Iani Chaos the primary GCM-wind stress orientation matches one of the several yardang populations, but both GCM vectors and yardang orientations are spread over a wide angular range (Fig. 9). In sites where multiple yardang populations occur, such as Iani Chaos, they are clustered into separate regions of homogeneous orientation. If unidirectional wind fields are required for yardang formation then yardangs could be formed in localised areas of unidirectional winds that are beyond the spatial resolution of the GCM. In modelled wind fields that show more than one dominant direction (e.g., Iani Chaos, Fig. 7) then one or more directions could be selectively halted or diverted by local topography in sub-regions, leaving some surfaces exposed to an effectively unidirectional erosion regime. This effect may explain

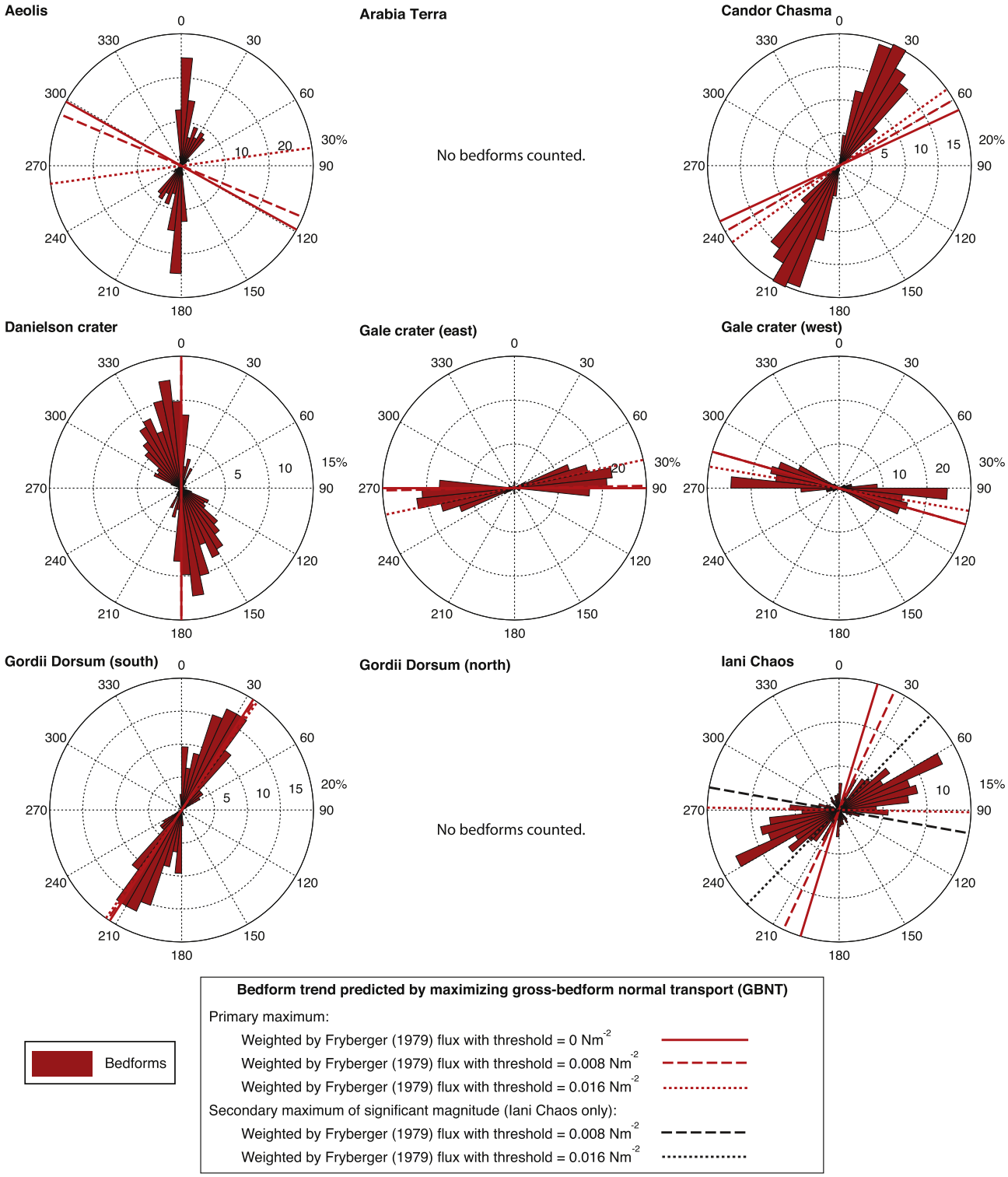

Fig. 8. Rose diagrams of trend lines representative of average bedform crest orientation. Angular bins are 6° and bar radii are sized according to percentage of the total population of each feature. Also shown are the results from two different methods for prediction of transverse bedform crest trends by maximising GBNT calculated from the MarsWRF GCM's annual vector wind field (Eq. (3)). For Iani Chaos, a secondary but significant local maxima in GBNT is also plotted (see Fig. 6).

observations of multiple yardang populations in close proximity that are oriented differently. For some locations, weighting of modelled wind vectors by u_*^5, instead of u_*^3, tends to produce a unidirectional 'spike' in the primary direction, but a greater angular dispersion for secondary directions (Fig. 7). In these cases (Gale crater east and west) yardangs are aligned with only the sharp primary direction, supporting the theory that yardang formation tends to occur only in effectively unidirectional wind fields.

5.3. Overall match of bedform and yardangs to GCM predictions

Poor matches between maximum GBNT and bedform orientation at Aeolis may be due to the choice of metric (GBNT, Fryberger, 1979, flux and threshold choice). However, the GCM spatial resolution of 2° is far lower than the bedforms themselves and hence may not represent the bedform-forming winds, especially in regions of complex topography where sub-grid cell topographic

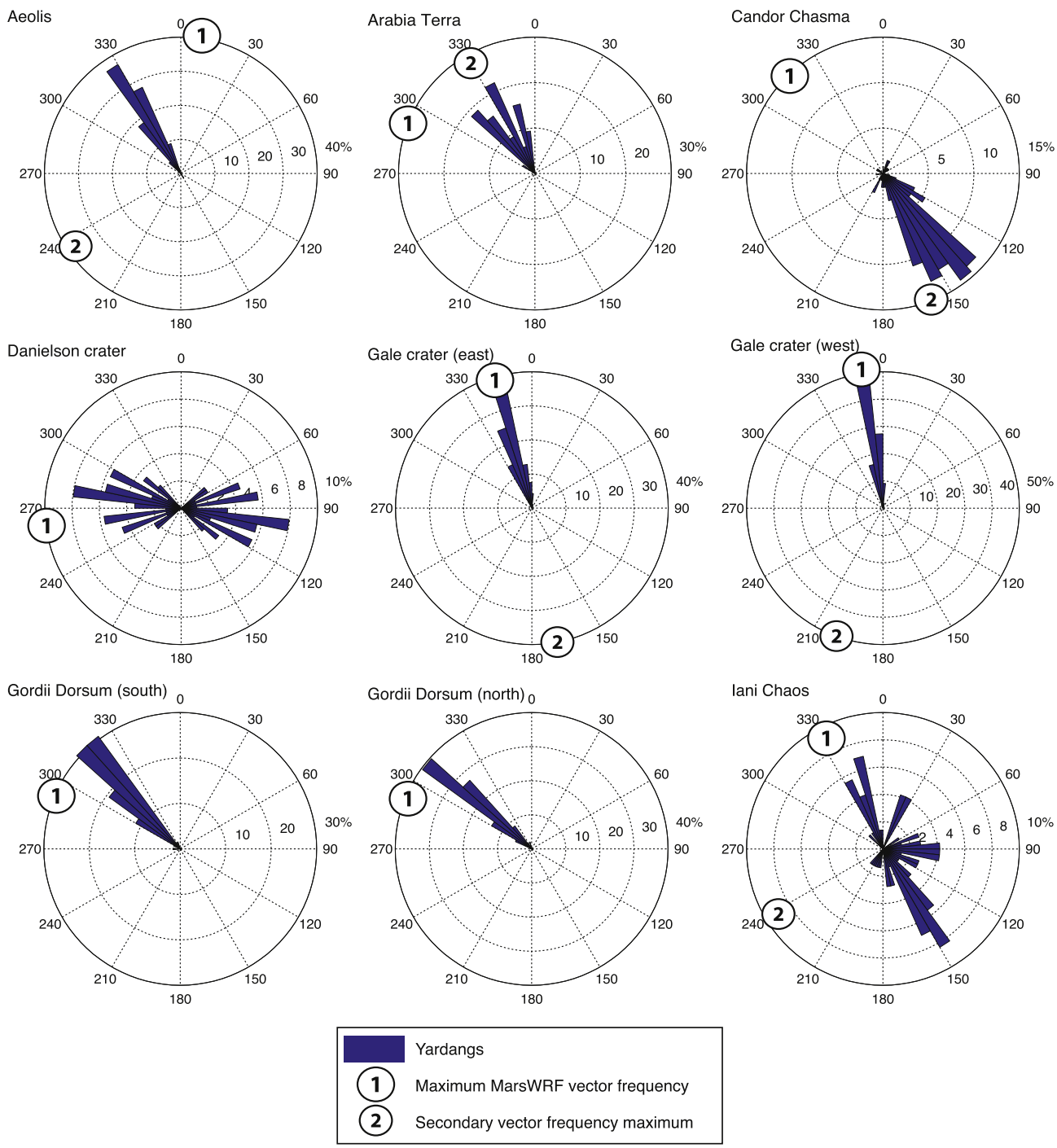

Fig. 9. Rose diagrams showing the orientation of yardang long axes (blue). Angular bins are 6° and bar radii are sized according to percentage of the total population of each feature. Also shown are the primary and secondary (where present) wind vector frequency maxima, derived from MarsWRF GCM's annual vector wind field shown in Fig. 7. Secondary orientations in dashed circles indicate directions prominent when low-order u_* weightings were applied. (For interpretation of the references to colour in this figure legend, the reader is referred to the web version of this article.)

diversion is not resolved. Localised bedform-forming winds may be better resolved using a higher spatial resolution mesoscale model, such as demonstrated by Rafkin and Michaels (2003) and Toigo and Richardson (2003).

If neither of these factors could be verified as responsible for the mismatch, and the present GCM resolves bedform-forming (and yardang-forming) winds, then assuming our choice of metric is an accurate bulk representation of the bedform development process, it would be possible to more confidently ascribe the offset as due to disequilibrium of both feature populations with the present-day wind regime. This would imply a more ancient origin for bedforms and yardangs under a different wind field. In any case, this site presents an opportunity for further study to investigate the impact of higher resolution mesoscale models.

We found no bedforms at the Arabia Terra or Gordii Dorsum (north) locations, but yardangs at Arabia Terra deviate approximately ~30° from the peak vector frequency of GCM winds, while those at Gordii Dorsum (south) show a better match with a deviation of ~10°.

At Gale crater (east and west) both bedforms and yardangs show excellent agreement between predicted and observed orientations, perhaps a surprising result given the variable local topography. Though at 2° lateral resolution the GCM does not resolve the detailed crater circulations that one might expect to strongly influence these bedforms. Indeed, image sequences from Mars Science Laboratory's NavCam show clouds at altitude moving towards 290–300° (Francis et al., 2013), which is in disagreement with modelled surface winds shown in Fig. 7. There is a strong possibility that our match is coincidental, rather than that crater circulation at Gale is dominated by regional flow, and a focus of ongoing work is using mesoscale (1.5 km resolution) modelling to assess the impact on predictions of crater flows, as resolved in modelling by Kite et al. (2013).

Observation of dune and ripple migration in NW Gale crater (Silvestro et al., 2013) supports a modern age for some bedforms in Gale but does not necessarily imply the same for bedforms in this study because their ripple locations do not coincide with our study areas. Proof that bedforms in our Gale study areas are in equilibrium with the present-day wind field could be sought through (1) observation of present-day bedform activity, and (2) agreement of mesoscale models with our GCM results.

Bedforms at Danielson crater show excellent agreement with maximised GBNT, while yardangs show poorer agreement, but still match within ~15°. Whereas yardang-forming winds predicted from GCM output are predominantly unidirectional, those that are unweighted and weighted by vector mean wind stress show a wide angular range and several significant maxima (Fig. 7). This could contribute to the uncertainty in determining unique yardang sense at this location, i.e., minor yardang erosion in a non-principle direction may have weathered direction specific-features.

Matches at Candor Chasma are seen between predicted orientations and bedforms (within ~25°) and yardangs (within ~10° of the secondary maximum marked '2'), however, this location is particularly susceptible to topographic influences and the validity of this apparent match remains to be tested with comparison to very high spatial resolution model output.

Gordii Dorsum (south) show similarly good matches with a slightly greater offset for yardangs. The significance of this offset remains to be tested, but could imply that yardangs are less in equilibrium with more modern bedform-forming wind regimes that are well represented by GCM output, or that the yardang-forming wind regime is not well captured by our interpretation of GCM output.

There is tentative agreement between the orientations of bedforms and some yardangs at Iani Chaos (Figs. 8 and 9), but there are additional yardang populations that may be representative of very localised unidirectional wind regimes unresolved by the GCM, or alternately by past wind fields. In either case, complex local topography warrants the use of a mesoscale model to resolve the variation in wind fields and therefore feature orientation over short distances.

At sites where bedforms are located between closely spaced yardangs wind channelling may artificially create an orthogonal relation between bedforms and yardangs. However, from our measurements we can only infer the surface winds at each site, not the unchannelled background wind field. We can only conclude that areas with dense yardang populations could bear a transient signature of past wind regimes, and through channelling, impose this transient wind field on bedforms in inter-yardang troughs.

The impact of major dust events was not considered in this initial work, and due to all the potential non-linear effects and feedbacks operating at different spatial scales we did not feel it would be useful to guess at the possible implications for results here, but dust effects will be considered in future studies.

6. Conclusions

We studied nine sites that are expected to be representative of modern day wind fields on Mars and measured the orientations of features with short (bedforms) and longer (yardangs) timescales of formation. We selected fine layered deposits because they are easily wind-eroded and therefore both harbour significant aeolian features and have young crater retention ages. Maximum crater retention ages derived for FLDs via comparison of crater size frequency distributions to those defined by Hartmann (2005) were found to be on the order of ~1–50 Ma, but could be underestimated by a factor of up to ~3, therefore placing them in loose agreement with previous estimates (available for Iani Chaos only: Warner et al., 2011), and confirming FLDs applicability to modern wind field determination. For sites where yardang and bedform orientations disagree, model ages represent an upper limit on yardang age and therefore timescales for changes in the local wind field.

Transverse bedforms were counted at 7 of 9 sites, while yardang orientations were analysed at all sites. Feature orientations were compared to output from the MarsWRF GCM running at a spatial resolution of 2°. Bedform orientations agreed very well with predictions made by maximising GBNT (Rubin and Hunter, 1987) and weighting by flux as defined by Fryberger (1979). Better agreements were generally observed when wind stress thresholds were applied, with the maximum applied threshold $\sigma_t = 0.016\ \mathrm{N\ m^{-2}}$ giving the best match for several sites. Application of wind stress thresholds had the greatest effect on predicted bedform orientation for sites with multi-directional wind fields. Sites with annually invariant, unidirectional wind fields showed no change with threshold. Poor agreement was seen for sites with extreme local topography such as chasma and chaos regions, implying that local topographic effects are important and therefore higher resolution mesoscale models are required before further model comparison can be made.

Yardang orientations agree well in most cases with a primary or secondary transport-weighted maxima in annual wind vector frequencies. Close inspection of maxima in weighted annual wind vector frequencies thus appears to provide a basis for meaningful prediction of yardang orientations in multidirectional wind fields in future studies. The agreement of multiple different yardang populations in close proximity with multiple maxima in an annual wind field may indicate local scale topographic blocking of some dominant wind directions and/or focusing of one, thus producing the highly unidirectional wind regime that appears required for yardangs to form.

The number of regions with good agreement between measured and predicted feature orientations by the MarsWRF GCM increases our confidence in using this model to predict winds elsewhere on Mars. Broadly, aeolian features on FLDs provide an excellent way to measure present-day wind directions and validate GCMs, however, care must be taken in areas of high topographic relief and higher resolution models are required to make more complete comparisons. We find that comparison of yardang long axes to directional maxima in modelled wind vector frequencies and comparison of bedform orientation to maximum GBNT are appropriate treatments. This work demonstrates an approach that could be used to gain quantitative insight into recent climate variations on Mars, so long as bedforms can be shown to be active in the present-day wind field.

Acknowledgments

Elliot Sefton-Nash and Nick Teanby are grateful for funding from the Leverhulme Trust for this work. Nick Teanby was also

funded by the UK Science and Technologies Facilities Council (STFC). Claire Newman was funded by NASA MFRP Grant No. NNX11AF59G, and all GCM simulations were performed on the High End Computing facility at NASA Ames.

References

Anderson, R.S., 1986. Erosion profiles due to particles entrained by wind: Application of an eolian sediment-transport model. Geol. Soc. Am. Bull. 97 (10), 1270–1278.

Andreotti, B., Claudin, P., Douady, S., 2002. Selection of dune shapes and velocities Part 1: Dynamics of sand, wind and barchans. Eur. Phys. J. B 28, 321–339.

Ansan, V., Loizeau, D., Mangold, N., Moulic, S.L., Carter, J., Poulet, F., Dromart, G., Lucas, A., Bibring, J.-P., Gendrin, A., Gondet, B., Langevin, Y., Masson, P., Murchie, S., Mustard, J., Neukum, G., 2011. Stratigraphy, mineralogy, and origin of layered deposits inside Terby crater, Mars. Icarus 211 (1), 273–304. http://dx.doi.org/10.1016/j.icarus.2010.09.011, ISSN 0019-1035.

Anthonsen, K.L., Clemmensen, L.B., Jensen, J.H., 1996. Evolution of a dune from crescentic to parabolic form in response to short-term climatic changes: Rabjerg Mile, Skagen Odde, Denmark. Geomorphology 17, 63–77.

Bagnold, R.A., 1941. The physics of blown sand and desert dunes. Methuen, New York.

Balme, M.R., Berman, D.C., Bourke, M.C., Zimbelman, J.R., 2008. Transverse aeolian ridges (TARs) on Mars. Geomorphology 101, 703–720.

Berman, D.C., Balme, M.R., Rafkin, S.C.R., Zimbelman, J.R., 2011. Transverse aeolian ridges (TARs) on Mars II: Distributions, orientations, and ages. Icarus 213, 116–130.

Bitter, J.G.A., 1963a. A study of erosion phenomena: Part 1. Wear 6, 5–21.

Bitter, J.G.A., 1963b. A study of erosion phenomena: Part 2. Wear 6, 169–190.

Bourke, M.C., Wilson, S.A., Zimbelman, J.R., 2003. The Variability of Transverse Aeolian Ridges in troughs on Mars. Lunar Planet. Sci. 34, 2090.

Bourke, M.C., Edgett, K.S., Cantor, B.A., 2008. Recent aeolian dune change on Mars. Geomorphology 94, 247–255.

Breed, C.S., Grolier, M.J., McCauley, J.F., 1979. Morphology and distribution of common 'sand' dunes on Mars: Comparison with the Earth. J. Geophys. Res. Solid Earth 84 (B14), 8183–8204. http://dx.doi.org/10.1029/JB084iB14p08183, ISSN 2156-220.

Bridges, N.T. et al., 2007. Windy Mars: A dynamic planet as seen by the HiRISE camera. Geophys. Res. Lett. 34 (23), 1–7. http://dx.doi.org/10.1029/2007GL031445, ISSN 1944-800.

Bridges, N.T. et al., 2012b. Planet-wide sand motion on Mars. Geology 40, 31–34.

Bridges, N.T., Ayoub, F., Avouac, J.-P., Leprince, S., Lucas, A., Mattson, S., 2012a. Earth-like sand fluxes on Mars. Nature 485, 339–342.

Cantor, B.A., Kanak, K.M., Edgett, K.S., 2006. Mars Orbiter Camera Observations of martian dust devils and their tracks (September 1997 to January 2006) and evaluation of theoretical vortex models. J. Geophys. Res. 111, E12002.

Catling, D.C., Wood, S.E., Leovy, C., Montgomery, D.R., Greenberg, H.M., Glein, C.R., Moore, J.M., 2006. Light-toned layered deposits in Juventae Chasma, Mars. Icarus 181 (1), 26–51, ISSN 0019-1035..

Chojnacki, M., Hynek, B.M., 2008. Geological context of water-altered minerals in Valles Marineris, Mars. J. Geophys. Res. (Planets) 113, E12005.

Chojnacki, M., Burr, D.M., Moersch, J.E., Michaels, T.I., 2011. Orbital observations of contemporary dune activity in Endeavor crater, Meridiani Planum, Mars. J. Geophys. Res. 116, E00F19.

Clarke, L.B., Werner, B.T., Okihiro, M., 2008. Surf zone megaripple orientation: Measurements and models. J. Geophys. Res. 113, C03018.

Claudin, P., Andreotti, B., 2006. A scaling law for aeolian dunes on Mars, Venus, Earth, and for subaqueous ripples. Earth Planet. Sci. Lett. 252, 30–44, ISSN 0012-821.

Daubar, I.J., McEwen, A.S., Byrne, S., 2013. How Accurately can We Date Recent Climate Change on Mars? Lunar Planet. Sci. 44, 2977.

Derickson, D., Kocurek, G., Ewing, R.C., Bristow, C., 2008. Origin of a complex and spatially diverse dune-field pattern, Algodones, southeastern California. Geomorphology 99, 186–204.

de Silva, S.L., Bailey, J.E., Mandt, K.E., Viramonte, J.M., 2010. Yardangs in terrestrial ignimbrites: Synergistic remote and field observations on Earth with applications to Mars. Planet. Space Sci. 58, 459–471.

Dundas, C.M., Keszthelyi, L.P., Bray, V.J., McEwen, A.S., 2010. Role of material properties in the cratering record of young platy-ridged lava on Mars. J. Geophys. Res., L12203.

Edgett, K.S., Blumberg, D.G., 1994. Star and linear dunes on Mars. Icarus 112 (2), 448–464. http://dx.doi.org/10.1006/icar.1994.1197, ISSN 0019-103.

Ewing, R.C., Peyret, G., Kocurek, G., Bourke, M.C., 2010. Dune field pattern formation and recent transporting winds in the Olympia Undae Dune Field, north polar region of Mars. J. Geophys. Res. 115, E08005.

Fenton, L.K., 2006. Dune migration and slip face advancement in the Rabe Crater dune field, Mars. Geophys. Res. Lett. 33 (20). http://dx.doi.org/10.1029/2006GL027133, ISSN 1944-8007.

Fenton, L.K., Richardson, M.I., 2001. Martian surface winds: Insensitivity to orbital changes and implications for aeolian processes. J. Geophys. Res. 106 (E12), 32,885–32,890.

Fenton, L.K., Toigo, A.D., Richardson, M.I., 2005. Aeolian processes in proctor crater on Mars: Mesoscale modeling of dune-forming winds. J. Geophys. Res. (Planets) 110, E06005.

Fenton, L.K., Michaels, T.I., Beyer, R.A., 2012. Aeolian Sediment Sources and Transport in Ganges Chasma, Mars: Morphology and Atmospheric Modeling. Lunar Planet. Sci., 43, 2441.

Flahaut, J., Quantin, C., Allemand, P., Thomas, P., 2010. Morphology and geology of the ILD in Capri/Eos Chasma (Mars) from visible and infrared data. Icarus 207 (1), 175–185. http://dx.doi.org/10.1016/j.icarus.2009.11.019, ISSN 0019-103.

Francis, R., et al., 2013. Observations of Clouds and Winds Aloft at Gale Crater. Lunar Planet. Sci. 44, 1717.

Fryberger, S.G., 1979. Dune forms and wind regime. In: McKee, E.D. (Ed.), U.S. Geological Survey Profile Pap. 1052, Washington, pp. 137–169.

Fueten, F. et al., 2010. Structural analysis of interior layered deposits in Northern Coprates Chasma, Mars. Earth Planet. Sci. Lett. 294, 343–356. http://dx.doi.org/10.1016/j.epsl.2009.11.004.

Gardin, E., Allemand, P., Quantin, C., Silvestro, S., Delacourt, C., 2012. Dune fields on Mars: Recorders of a climate change? Planet. Space Sci. 60 (1), 314–321, ISSN 0032-063.

Golombek, M. et al., 2010. Constraints on ripple migration at Meridiani Planum from opportunity and HiRISE observations of fresh craters. J. Geophys. Res. 115, E00F08.

Greeley, R. et al., 1982. Rate of wind abrasion on Mars. J. Geophys. Res. 87 (12), 9–24.

Greeley, R., Iversen, J.D., 1985. Wind as a Geological Process on Earth, Mars. Venus and Titan. Cambridge University Press.

Greeley, R., Skypeck, A., Pollack, J.B., 1993. Martian aeolian features and deposits: Comparisons with general circulation model results. J. Geophys. Res. 98 (E2), 3183–3196. http://dx.doi.org/10.1029/92JE02580, ISSN 2156-2202.

Haberle, R.M. et al., 1993. Mars atmospheric dynamics as simulated by the NASA Ames General Circulation Model: 1. The zonal-mean circulation. J. Geophys. Res. (Planets) 98 (E2), 3093–3123. http://dx.doi.org/10.1029/92JE02946, ISSN 2156-2202.

Hartmann, W.K., 1999. Martian cratering VI: Crater count isochrons and evidence for recent volcanism from Mars Global Surveyor. Meteorit. Planet. Sci. 34, 167–177.

Hartmann, W.K., 2005. Martian cratering 8: Isochron refinement and the chronology of Mars. Icarus 174, 294–320.

Hayward, R.K. et al., 2007. Mars global digital dune database and initial science results. J. Geophys. Res. 112, E11007.

Hayward, R.K., Titus, T.N., Michaels, T.I., Fenton, L.K., Colaprete, A., Christensen, P.R., 2009. Aeolian dunes as ground truth for atmospheric modeling on Mars. J. Geophys. Res. (Planets) 114, E11012.

Hobbs, S.W., Paull, D.J., Bourke, M.C., 2010. Aeolian processes and dune morphology in Gale Crater. Icarus 210, 102–115.

Ivanov, A.B., Melosh, H.J., McEwen, A.S., The HiRISE Team, 2008. Small Impact Crater Clusters in High Resolution HiRISE Images. Lunar Planet. Sci. 39, 1221.

Kite, E.S., Lewis, K.W., Lamb, M.P., Newman, C.E., Richardson, M.I., 2013. Growth and form of the mound in Gale Crater, Mars: Slope wind enhanced erosion and transport. Geology 41 (5), 543–546.

Kok, J., 2010. An improved parameterization of wind-blown sand flux on Mars that includes the effect of hysteresis. Geophys. Res. Lett. 37 (L12202), 1–6.

Lancaster, N., 1991. The orientation of dunes with respect to sand-transporting winds: A test of Rubin and Hunter's gross bedform-normal rule. Acta Mech. Suppl. 2, 89–102.

Lancaster, N., Nickling, W.G., Gillies, J.A., 2010. Sand transport by wind on complex surfaces: Field studies in the McMurdo Dry Valleys, Antarctica. J. Geophys. Res. (Earth Surface) 115, F03027. http://dx.doi.org/10.1029/2009JF001408.

Lee, P., Thomas, P.C., 1995. Longitudinal dunes on Mars: Relation to current wind regimes. J. Geophys. Res. (Planets) 100 (E3), 5381–5395. http://dx.doi.org/10.1029/95JE00225, ISSN 2156-220.

B.K. Lucchitta, et al., The Canyon system on Mars, in: Mars, Kieffer H.H., Jakosky, B.M., Snyder, C.W. and Matthew, M.S. (Eds.), University of Arizona Press: Tuscon, 1992, pp. 453–492.

Malin, M.C., Edgett, K.S., 2000. Sedimentary rocks of early Mars. Science 290, 1927–1937.

Malin, M.C., Edgett, K.S., Posiolova, L.V., McColley, S.M., Noe Dobrea, E.Z., 2006. Present-day impact cratering rate and contemporary gully activity on Mars. Science 314, 1573–1577.

McEwen, A.S. et al., 2007. Mars reconnaissance Orbiter's High Resolution Imaging Science Experiment (HiRISE). J. Geophys. Res. 112, E05S02.

McEwen, A.S., Bierhaus, E.B., 2006. The importance of secondary cratering to age constraints on planetary surfaces. Ann. Rev. Earth Planet. Sci. 34, 535–567.

McEwen, A.S., Preblich, B.S., Turtle, E.P., Artemieva, N.A., Golombek, M.P., Hurst, M., Kirk, R.L., Burr, D.M., Christensen, P.R., 2005. The rayed crater Zunil and interpretations of small impact craters on Mars. Icarus 176, 351–381.

A.S. McEwen, M.E. Banks, N. Baugh, K. Becker, A. Boyd, J.W. Bergstrom, R.A. Beyer, E. Bortolini, N.T. Bridges, S. Byrne, B. Castalia, F.C. Chuang, L.S. Crumpler, I. Daubar, A.K. Davatzes, D.G. Deardorff, A. DeJong, W.A. Delamere, E.N. Dobrea, C.M. Dundas, E.M. Eliason, Y. Espinoza, A. Fennema, K.E. Fishbaugh, T. Forrester, P.E. Geissler, J.A. Grant, J.L. Griffes, J.P. Grotzinger, V.C. Gulick, C.J. Hansen, K.E. Herkenhoff, R. Heyd, W.L. Jaeger, D. Jones, B. Kanefsky, L. Keszthelyi, R. King, R.L. Kirk, K.J. Kolb, J. Lasco, A. Lefort, R. Leis, K.W. Lewis, S. Martinez-Alonso, S. Mattson, G. McArthur, M.T. Mellon, J.M. Metz, M.P. Milazzo, R.E. Milliken, T. Motazedian, C.H. Okubo, A. Ortiz, A.J. Philippoff, J. Plassmann, A. Polit, P.S. Russell, C. Schaller, M.L. Searls, T. Spriggs, S.W. Squyres, S. Tarr, N. Thomas, B.J. Thomson, L.L. Tornabene, C.V. Houten, C. Verba, C.M. Weitz, J.J. Wray, The High Resolution Imaging Science Experiment (HiRISE) during MRO's Primary Science

Phase (PSP), Icarus 205 (1) (2010) 2–37, doi:10.1016/j.icarus.2009.04.023. ISSN 0019-1035
McKee, E.D., 1979. A study of global sand seas, Professional paper 1052, United States Geological Survey.
Merrison, J. et al., 2008. An environmental simulation wind tunnel for studying Aeolian transport on Mars. Planet. Space Sci. 56, 426–437. http://dx.doi.org/10.1016/j.pss.2007.11.007, ISSN 0032-0633.
Monin, A.S., Obukhov, A.M., 1954. Basic laws of turbulent mixing in the surface layer of the atmosphere. Tr. Akad. Nauk SSSR Geofiz. Inst. 24, 163–187.
Moore, H.J., 1985. The martian dust storm of Sol 1742. J. Geophys. Res. (Planets) 90 (S01), 163–174. http://dx.doi.org/10.1029/JB090iS01p00163, ISSN 2156-220.
Newman, C.E., Lewis, S.R., Read, P.L., 2005. The atmospheric circulation and dust activity in different orbital epochs on Mars. Icarus 174 (1), 135–160.
Newman, C.E., Richardson, M.I., Lancaster, N., Rubin, D.M., 2012. General circulation model predictions of dunes on Mars and Titan using planetWRF. In: Third International Planetary Dunes Workshop, Flagstaff, AZ.
Okubo, C.H., 2010. Structural geology of Amazonian-aged layered sedimentary deposits in southwest Candor Chasma, Mars. Icarus 207, 210–225.
Okubo, C.H., Lewis, K.W., McEwen, A.S., Kirk, R.L., 2008. Relative age of interior layered deposits in southwest Candor Chasma based on high-resolution structural mapping. J. Geophys. Res. 112, E12002.
Popova, O., Nemtchinov, I., Hartmann, W.K., 2003. Bolides in the present and past martian atmosphere and effects on cratering processes. Meteorit. Planet. Sci. 38 (6), 905–925.
Rafkin, S.C.R., Michaels, T.I., 2003. Meteorological predictions for 2003 Mars Exploration Rover high-priority landing sites. J. Geophys. Res. 108, E12.
Reffet, E., Courrech du Pont, S., Hersen, P., Douady, S., Fulchignoni, M., 2008. Longitudinal dunes on Titan: A laboratory approach. In: Planetary Dunes Workshop: A Record of Climate Change, held April 29–May 2, 2008 in Alamogordo, New Mexico. LPI Contribution No. 1403, pp. 58–59.
Richardson, M.I., Toigo, A.D., Newman, C.E., 2007. PlanetWRF: A general purpose, local to global numerical model for planetary atmospheric and climate dynamics. J. Geophys. Res. (Planets) 112, E9. http://dx.doi.org/10.1029/2006JE002825, ISSN 2156-2202.
Rubin, D.M., Hunter, R.E., 1987. Bedform alignment in directionally varying flows. Science 237, 276–278.
Rubin, D.M., Tsoar, H., Blumberg, D., 2008. A second look at western Sinai seif dunes and their lateral migration. Geomorphology 93, 335–342.
Sefton-Nash, E., Catling, D.C., Wood, S.E., Grindrod, P.M., Teanby, N.A., 2012. Topographic, spectral and thermal inertia analysis of interior layered deposits in Iani Chaos, Mars. Icarus 221, 20–42.
Silvestro, S. et al., 2013. Pervasive aeolian activity along rover Curiosity's traverse in Gale Crater, Mars. Geology 41, 483–486. http://dx.doi.org/10.1130/G34162.1.
Silvestro, S., Fenton, L.K., Vaz, D.A., Bridges, N.T., Ori, G.G., 2010. Ripple migration and dune activity on Mars: Evidence for dynamic wind processes. Geophys. Res. Lett. 37, L20203.
Silvestro, S., Vaz, D.A., Fenton, L.K., Geissler, P.E., 2011. Active aeolian processes on Mars: A regional study in Arabia and Meridiani Terrae. Geophys. Res. Lett. 38 (20), 1–6. http://dx.doi.org/10.1029/2011GL048955, ISSN 1944-800.
Sullivan, R. et al., 2005. Aeolian processes at the Mars Exploration Rover Meridiani Planum landing site. Nature 436 (7047), 58–61, ISSN 0028-083.
Sullivan, R., et al., 2007. Aeolian Geomorphology with MER Opportunity at Meridiani Planum, Mars. Lunar Planet. Sci. 38, 2048.
Toigo, A.D., Richardson, M.I., 2003. Meteorology of proposed Mars Exploration Rover landing sites. J. Geophys. Res. 108, E12.
Toigo, A.D., Lee, C., Newman, C.E., Richardson, M.I., 2012. The impact of resolution on the dynamics of the martian global atmosphere: Varying resolution studies with the MarsWRF GCM. Icarus 221 (1), 276–288. http://dx.doi.org/10.1016/j.icarus.2012.07.020, ISSN 0019-103.
Ward, W.R., 1979a. Present obliquity oscillations of Mars: Fourth-order accuracy in orbital e and I. J. Geophys. Res. Solid Earth 84 (B1), 237–241. http://dx.doi.org/10.1029/JB084iB01p00237, ISSN 2156-2202.
Ward, A.W., 1979b. Yardangs on Mars: Evidence of recent wind erosion. J. Geophys. Res. 84 (B14), 8147–8166.
Warner, N.H. et al., 2011. Constraints on the origin and evolution of Iani Chaos, Mars. J. Geophys. Res. (Planets) 116 (E06003), 1–29.
Wu, J., Wang, Y., Cheng, H., 2009. Bedforms and bed material transport pathways in the Changjiang (Yangtze) Estuary. Geomorphology 104 (3–4), 175–184.
Zimbelman, J.R., 2010. Transverse aeolian ridges on Mars: First results from HiRISE images. Geomorphology 121, 22–29.
Zuber, M.T. et al., 1992. The Mars observer laser altimeter investigation. J. Geophys. Res. 97 (E5), 7781–7797.